JOURNAL OF COMPUTATIONAL PHYSICS 90, 98–122 (1990)

An Eigenfunction Analysis of Axisymmetric Jet Flow

M. KIRBY, J. BORIS,* AND L. SIROVICH

Center for Fluid Mechanics, Brown University, Providence, Rhode Island 02912

Received October 24, 1988; revised July 14, 1989

The *snapshot method* is used to analyze a large eddy simulation of axisymmetric jet flow. An ensemble of realizations is collected using a sampling condition that corresponds to the passage of a large scale vortex at a position six diameters downstream from the nozzle. The analysis is performed separately on a variable composed of the primitive flow quantities and the mass fraction of the material originally emerging from the jet nozzle. The fraction of the *energy* contained by the first ten eigenfunctions in each case is 94% and 80%. A 10-term expansion captures the large scale features of an arbitrary flow.

1. INTRODUCTION

Numerous investigations, beginning with the work of Townsend [1] and Theodorsen [2] in the mid 1950s, have clearly established the existence of coherent large-scale motions in transitional and turbulent flows. Brown and Roshko's well-known result for the plane mixing layer [3] provides a striking example of this. The articles of Cantwell [4], Hussain [5, 6], and Feidler [7] examine and review the role of coherent structures in turbulent flows and attempt to incorporate them into turbulence theory. Studies investigating the nature of laboratory jet flow corroborate the existence of large-scale structure, e.g., [8–12]. The presence of these highly organized patterns suggests the possibility that a reduced parametrization, or amount of information, can be used to quantify the flow.

In this investigation we examine the application of the *snapshot method* [13–16] to an ensemble of conditionally sampled flow realizations produced by a large eddy simulation of an axisymmetric jet. The analytical methods based on the proper orthogonal decomposition (known in pattern theory as the Karhunen–Loéve (K-L) expansion) are especially useful for efficiently characterizing an ensemble of inhomogeneous patterns which possess a high degree of organized structure. Lumley proposed the proper orthogonal decomposition [17–19] as an unbiased method for extracting coherent structures, however, the degree to which the resulting structures correspond to those found in experiment is largely unconfirmed. An

* Naval Research Laboratory, Washington, DC 20375.

0021-9991/90 $3.00

application of Lumley's decomposition to estimated cross-spectra in laboratory jet flow found that several modes were necessary to realistically capture the flow structure [20].

The K-L expansion, outlined in Section 4, provides a low-dimensional representation of a characteristic large scale structure by decomposing it into a set of uncorrelated, data-dependent components. These components are the eigenfunctions of a two-point correlation tensor and they frorm an *optimal* basis in several senses. For instance, the K-L eigenfunctions minimize the mean-square error of the expansion, maximize the total energy captured in each coordinate direction, subject to orthogonality constraints and form a complete basis with which to represent the flow. Also, while the method is optimal with respect to second order moments, there is no loss of higher order moment information as the basis is complete. However, in general the efficiency with which higher order information is captured is not optimized by the K-L expansion. For a full discussion of these and other properties of the K-L expansion there exist many detailed references [21–26].

This approach provides a concrete mathematical framework in which to discuss the high-energy components of the flow and may potentially provide a reduced dynamical model. The expansion allows the characterization and data compressed representation of a flow realization in terms of a fixed set of *eigenflows*. While these eigenflows are not in general solutions of the flow equations they can clearly be viewed as corresponding to mechanical motions and as such provide insight into the relative make up of each flow realization in terms of its *eigenstructure*. When the flow is decomposed in this manner, pictorially we see that its large-scale features are captured using a small number of eigenfunctions.

Appropriate methods for extracting, or educing, coherent structure from turbulent flow is an area of active research. Early visualization techniques have been supplanted by more objective statistical or feature based approaches. For example, the VITA technique of Blackwelder and Kaplan [27], the quadrant analysis of Lu and Willmarth [28], and Adrian's application of stochastic estimation [29]. Also, in the case of jet flow, structures have been induced by periodic forcing which excites a *preferred mode* [8]. The number of methods for educing coherent structures reflects the lack of a generally accepted rigorous definition of what they are. A better understanding of the composition of *observed* structures is clearly necessary for any such deliberations to proceed. With this as a goal, our study focuses on large-scale vortices and their composition in terms of the K-L eigenfunctions. In this spirit, we apply the conditional sampling procedure, described in Section 3, which eliminates the shifting of experimental data used to condition the ensemble for the randomly timed snapshots in [30].

One potential side benefit of this study is the comparison of the low-dimensional representations of experimental and computational flows. In Section 6 we consider the results of an analogous study of a qualitatively similar laboratory flow [30]. In general, this type of comparison promises to be highly complimentary for the following reasons: It is typical of a numerical simulation to obtain highly detailed data but over limited time intervals; experiments, on the other hand, produce data

for much longer time periods but generally with limited detail. Clearly, any connections or relationships we can infer between the mechanical motions provided by the machine flow and the concentration fields of the experiment may serve to mutually benefit each approach.

With this goal in mind, we computed not only the primitive flow variables for the jet, but also the mass fraction, a variable analogous to the gas concentration fields produced by the experiment previously mentioned. Clearly this is an idealization, as the experiment produces 2D slices of a truly 3D flow while the simulation is axisymmetric. However, data for the experimental jet, as well as the simulation, were collected in the transition region where 2D effects are dominant.

It is well known that the method employed here requires abundant data to provide sufficient statistics for the computation of the eigenfunctions. The axisymmetric jet was modeled using an highly efficient large eddy simulation based on an optimized FCT algorithm [31] which was completely vectorized/parallelized. This enabled the generation of a reasonably sized ensemble of flow realizations, each member of which satisfies a sampling condition. Details of the simulation are given in Section 2. In theory it is a simple matter to extend all of the techniques applied here to 3D flows; currently however, this would be an expensive proposition in light of the fact that the approach requires a statistically large database. Yet, large eddy simulations of 3D shear flows have previously been carried out for a small number of realizations using FCT, e.g., [32].

2. Numerical Simulation

Air at standard temperature and pressure is passed through a cylindrical jet with a velocity of 150 m/s and nozzle diameter 5 cm into background air (also at STP) initially at rest. This corresponds to a Reynolds number, based on the jet diameter, of $O(10^4)$. Typical flow realizations produced by the simulation are shown in Figs. 1 and 2. The axis of symmetry is the bottom edge of the flow. The numerical simulation generates the pressure p, internal energy E, density ρ, and horizontal and vertical momentum densities ρu as the primitive variables along with one derived variable, i.e., the mass fraction σ. To make the analysis convenient we will interchangeably consider the flow variables to be either scalar functions of $\mathbf{x}$, or arrays defined on a discrete computational grid.

The numerical simulation solves the time-dependent compressible conservation equations for an ideal gas in axisymmetric geometry,

$$\frac{\partial \rho}{\partial t} + \frac{\partial}{\partial z}(\rho u_z) + \frac{1}{r}\frac{\partial}{\partial r}(r\rho u_r) = 0, \tag{1.1}$$

$$\frac{\partial}{\partial t}(\rho u_r) + \frac{\partial}{\partial z}(\rho u_r u_z) + \frac{1}{r}\frac{\partial}{\partial r}(r\rho u_r u_r) + \frac{\partial P}{\partial r} = 0, \tag{1.2}$$

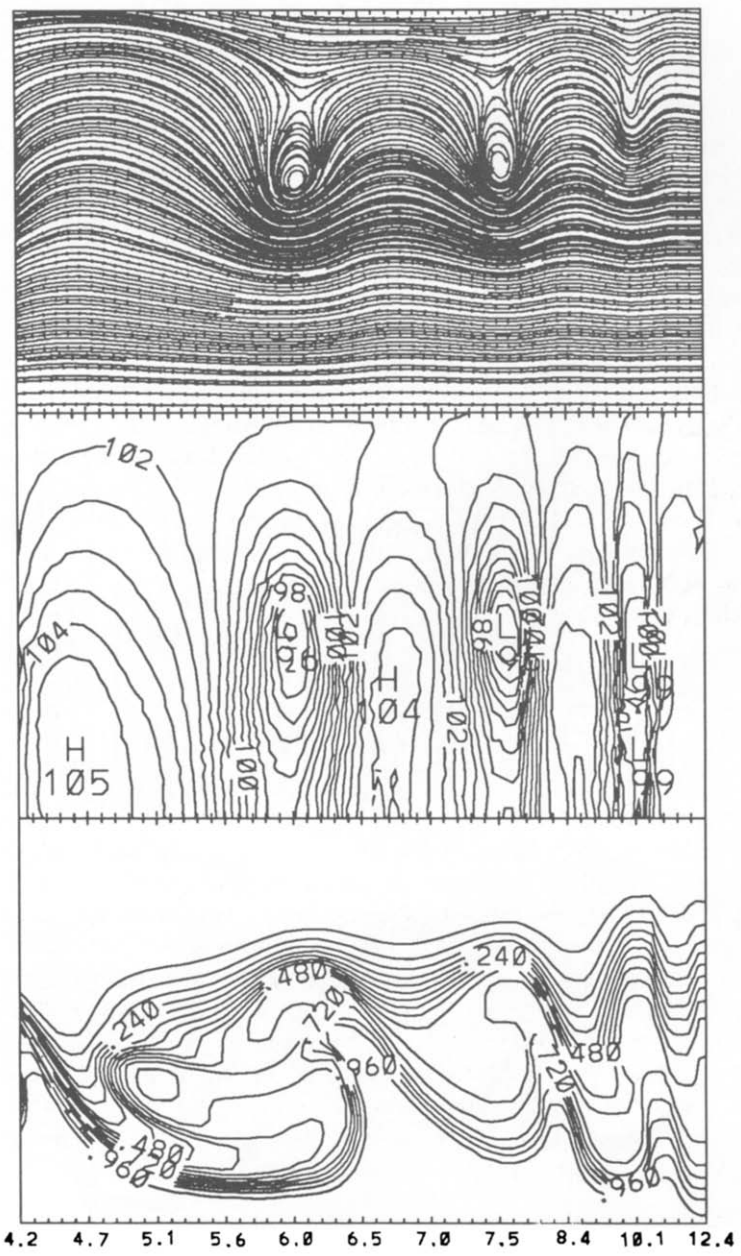

FIG. 1. Top: Instantaneous streamlines of a typical flow realization. Center: Corresponding pressure field. Bottom: Mass fraction. This snapshot is included in the ensemble.

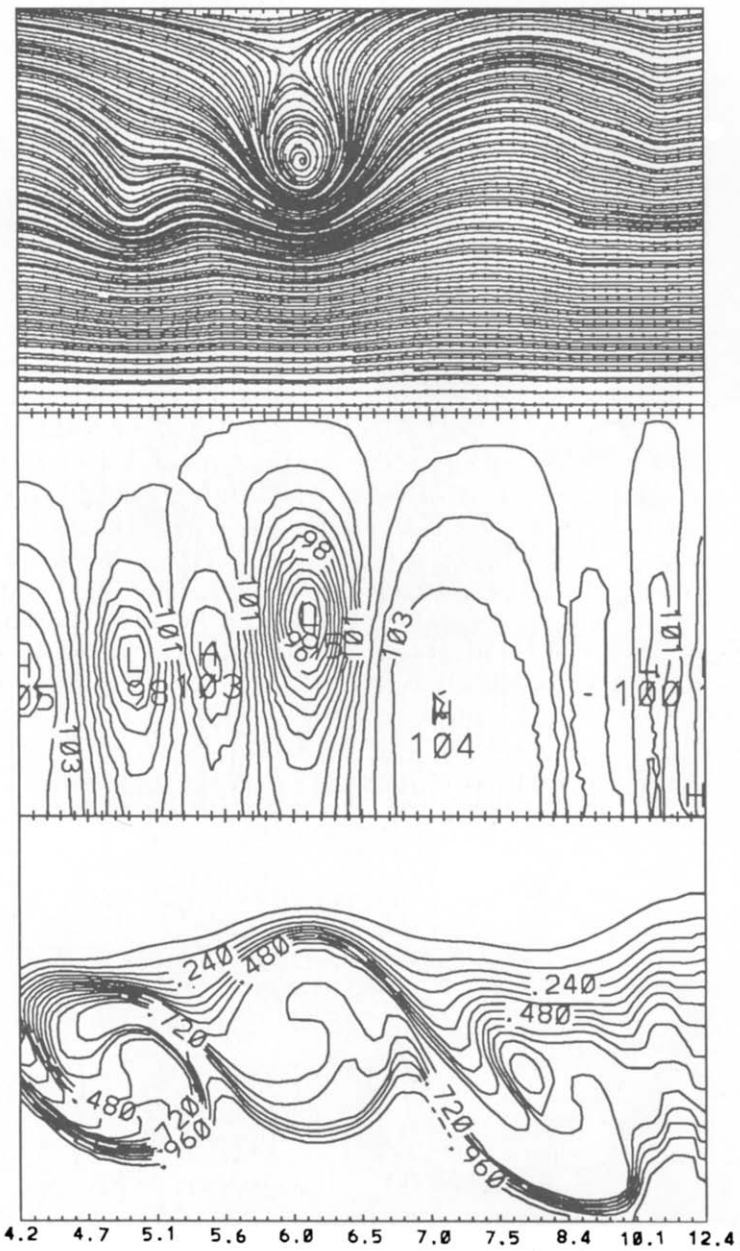

FIG. 2. Top: Instantaneous streamlines of a second typical flow realization. Center: Corresponding pressure field. Bottom: Mass fraction. This snapshot is *not* included in the ensemble.

$$\frac{\partial}{\partial t}(\rho u_z) + \frac{\partial}{\partial z}(\rho u_z u_z) + \frac{1}{r}\frac{\partial}{\partial r}(r\rho u_z u_r) + \frac{\partial P}{\partial z} = 0, \tag{1.3}$$

$$\frac{\partial E}{\partial t} + \frac{\partial}{\partial z}((E+P)u_z) + \frac{1}{r}\frac{\partial}{\partial r}(ru_r(E+P)) = 0. \tag{1.4}$$

The energy is $E = P/(\gamma - 1) + \frac{1}{2}\rho(u_r^2 + u_z^2)$, where γ denotes the ratio of specific heats. The flow is assumed to be inviscid and non-heat conducting. The mass fraction σ is computed at each time step by

$$\frac{\partial \sigma}{\partial t} + \nabla \cdot (\mathbf{u}\sigma) = 0 \tag{1.5}$$

As mentioned earlier, the mass fraction is analogous to the concentration field measured in the seeded jet experiment [30] and is obtained by tagging particles that make up the jet material and applying a conservation law which allows us to follow their progress. The computations are carried out on a 240 by 80 grid, corresponding to 12.4 jet diameters length of flow. The computational grid is uniform for the first 7.2 diameters after which it is stretched to take advantage of the fact that fewer cells are required to describe the evolution of the large-scale structure. Two-dimensional solutions are constructed using direction splitting and time step splitting with a one-dimensional, fourth-order, phase accurate flux-corrected transport (FCT) algorithm [31]. No explicit subgrid turbulence model is included because the FCT algorithm acts effectively as a high-frequency filter which diffuses the smallest scale structures which are not adequately described with the grid resolution chosen. The numerical viscosity inherent in the algorithm mimics the behavior of small scale turbulent diffusion at high Reynolds numbers by smoothing small scale structures on the order of a few computational cells [33].

3. Preliminaries: Sampling, Mean Subtraction

In order to obtain independent events representing the same type of coherent structure we select only *snapshots* that satisfy a predetermined strobe condition. The sampling condition is specified as follows: the radial distance from the axis of the jet, at a position six diameters downstream of the nozzle, to the point where the value of the mass fraction one-half is measured; when this distance passes through a maximum the flow is sampled. The condition corresponds to the passage of a large scale vortex. Since the actual strobing of the flow took place at unequal intervals we infer, as expected, that the flow is not periodic. The computer simulation was carried out for 2×10^5 timesteps giving 58 snapshots that satisfied the ensemble strobe condition. This corresponds to 100 to 150 vortex sheddings at the nozzle lip since some merging has taken place at the strobe location. The sampling began after the flow was fully initialized, i.e, after about 40,000 time steps. The region of our analysis will be 4.2 to 12.4 diameters downstream.

Ensemble averages are computed according to, e.g.,

$$\bar{\sigma}(\mathbf{x}) = \frac{1}{M} \sum_{n=1}^{M} \sigma^{(n)}(\mathbf{x}) = \langle \sigma^{(n)}(\mathbf{x}) \rangle, \tag{2}$$

where M is the number of snapshots in the ensemble. Throughout the rest of this paper we focus on the fluctuating quantities of the flow variables, e.g., the fluctuating mass fraction is given by

$$\sigma'(\mathbf{x}) = \sigma(\mathbf{x}) - \bar{\sigma}(\mathbf{x}). \tag{3}$$

However, for convenience we drop the primed notation.

4. Karhunen–Loève Expansion

4.1. *Formulation*

The Karhunen–Loève expansion is based on representing a typical realization of a flow in terms of the eigenfunctions of the integral equation

$$K_{ij}(\mathbf{x}, \mathbf{x}')\, w_j^{(n)}(\mathbf{x}') = \lambda^{(n)}\, w_i(\mathbf{x}), \tag{4}$$

where summation and integration conventions are assumed. The two point covariance tensor is defined by

$$K_{ij}(\mathbf{x}, \mathbf{x}') = \langle U_i(\mathbf{x})\, U_j(\mathbf{x}') \rangle, \tag{5}$$

where

$$\mathbf{U} = (\rho u, \rho v, p) \tag{6}$$

and the brackets indicate the ensemble average.

The analysis for the derived variable, i.e., the mass fraction, is carried out separately and parallels the above discussion. In this case (4) becomes

$$K(\mathbf{x}, \mathbf{x}')\, \omega^{(n)}(\mathbf{x}') = \lambda^{(\omega)}\, \omega^{(n)}(\mathbf{x}), \tag{7}$$

where K is given by

$$K(\mathbf{x}, \mathbf{x}') = \langle \sigma(\mathbf{x})\, \sigma(\mathbf{x}') \rangle. \tag{8}$$

In each case the kernel K is symmetric and nonnegative thus we have orthogonal eigenfunctions and non-negative eigenvalues. The kernels are also degenerate, a fact which greatly simplifies the actual computation of (4) and (7). In addition, the cost of the calculation increases only linearly with the number of flow variables concatenated in (6).

Once we have computed the eigenfunctions, we can *reconstruct* a member of the ensemble by an N term expansion with

$$\mathbf{U}^N = \sum_{k=1}^{N} a^{(k)}\mathbf{w}^{(k)}, \tag{9}$$

where

$$a_k = (\mathbf{U}, \mathbf{w}^{(k)}), \tag{10}$$

under the normal Euclidean inner product.

When $N = M$ this reconstruction is exact, since in this case the expansion is equivalent to a linear change of basis. The error introduced when the series is truncated must be interpreted carefully since in practice it is improbable that an ensemble will be large enough to characterize, to arbitrary accuracy, all possible flows that satisfy the strobe condition. Since we do not know in advance how large an ensemble will be large enough, this error is underestimated and hence of limited value. More importantly, we can estimate the error of the *approximation* of a snapshot that satisfies the strobe condition but which was not included in our original ensemble. The degree to which we are successful in approximating these flows will tell us to what extent our optimal basis actually spans our solution set [34].

We use the Euclidean distance between the exact fluctuating flow field ϕ and its N term expansion $\mathbf{U}^N$,

$$E_N = \frac{\|\mathbf{U}^N - \mathbf{U}\|}{\|\mathbf{U}\|} \tag{11}$$

as a quantitative measure of the error of the approximation.

4.2. *Scaling*

Since we have concatenated variables measured in different units with different variances we must introduce appropriate scale factors to prevent the domination of any one flow variable in the computation of the eigenfunctions. With this in mind we determine three scale factors which force the magnitude of the fluctuating variables to be, on average, $O(1)$. For example, we compute the pressure scale factor by

$$s_p = 1/\langle \sqrt{(1/N_h N_v) \textstyle\sum_{ij}^{N_h N_v} p_{ij}^{(k)}} \rangle. \tag{12}$$

Here $N_h = 115$ and $N_v = 70$ represent the grid resolution in the horizontal and vertical directions, respectively (for the region 4.5 to 12.4 diameters downstream). Similar scale factors are computed for the momentum density components.

5. RESULTS

5.1. *Ensemble Averages and Fluctuating Quantities*

The ensemble averages of the momentum density, pressure, and mass fraction are shown in Fig. 3. We see that there is indeed a well-resolved vortex at the strobe location and a corresponding minimum in the pressure distribution. Also, the strobe condition manifests itself in the ensemble average of the mass fraction as we see the mass fraction contour of $\sigma = 0.5$ is in fact a well defined peak.

Examining the fluctuating fields of the flows shown in Figs. 4 and 5 it is apparent that they have well defined, distinguishing large-scale structure. For instance, the fluctuating momentum density field shown in Fig. 4 consists of a complicated pattern of vortices, one of which is significantly stronger than the others. The momentum density field shown in Fig. 5 has four well defined vortices of approximately the same strength. Corresponding differences are exhibited in the other flow variables. Thus it is established that the flows represent widely different, complex behavior and the degree to which they can be accurately represented will provide a good test for the method.

5.2. *Eigenvalues*

The eigenvalues (normalized by the total sum of the eigenvalues) resulting from Eqs. (4) and (7) are shown in Fig. 6. The conventional global Karhunen–Loéve estimate of the dimensionality [16] of the set of snapshots, i.e., the index i of the eigenvalue for which $D^{(i)} = \lambda^{(i)}/\lambda_{\max} = 0.01$, is 15 for the composed variable. The dimensionality estimate for the mass fraction is 31. This should be compared with an estimate of 41 for the concentration fields of the seeded jet [30]. From this we can infer that the structure of the particle paths is more complicated than that of the velocity and pressure fields. Also, it follows that the information describing the particle paths is spread over a larger range of scales.

It is useful to consider the fraction of variance q_N contained, on average, in the expansion for a given number of terms, where

$$q_N = \frac{\sum_{k=1}^{N} \lambda^{(k)}}{\sum_{k=1}^{2M} \lambda^{(k)}}. \tag{13}$$

This gives us information that $D^{(i)}$ does not, since it tells us how much information is contained in the tail of the expansion.

The quantity q_N is plotted versus N for the eigenvalues of both (4) and (7) in Fig. 7. We see that for the composed variable five terms contain 85% of the variance and for the mass fraction 65% of the variance. These figures are up to 94% and 80% by 10 terms. However, it should be kept in mind that these figures will probably go down if we had more realizations in the ensemble. This is to be expected, since we have not completely spanned our space of admissible solutions by our limited data set. Ideally, if we kept adding snapshots the quantity q_N^M would tend to a limit as M goes to infinity. In the case of the seeded jet, where we had

FIG. 3. Top: Instantaneous streamlines of ensemble averaged velocity field. Center: Ensemble averaged pressure field. Bottom: Ensemble averaged mass fraction. Ensemble size = 55.

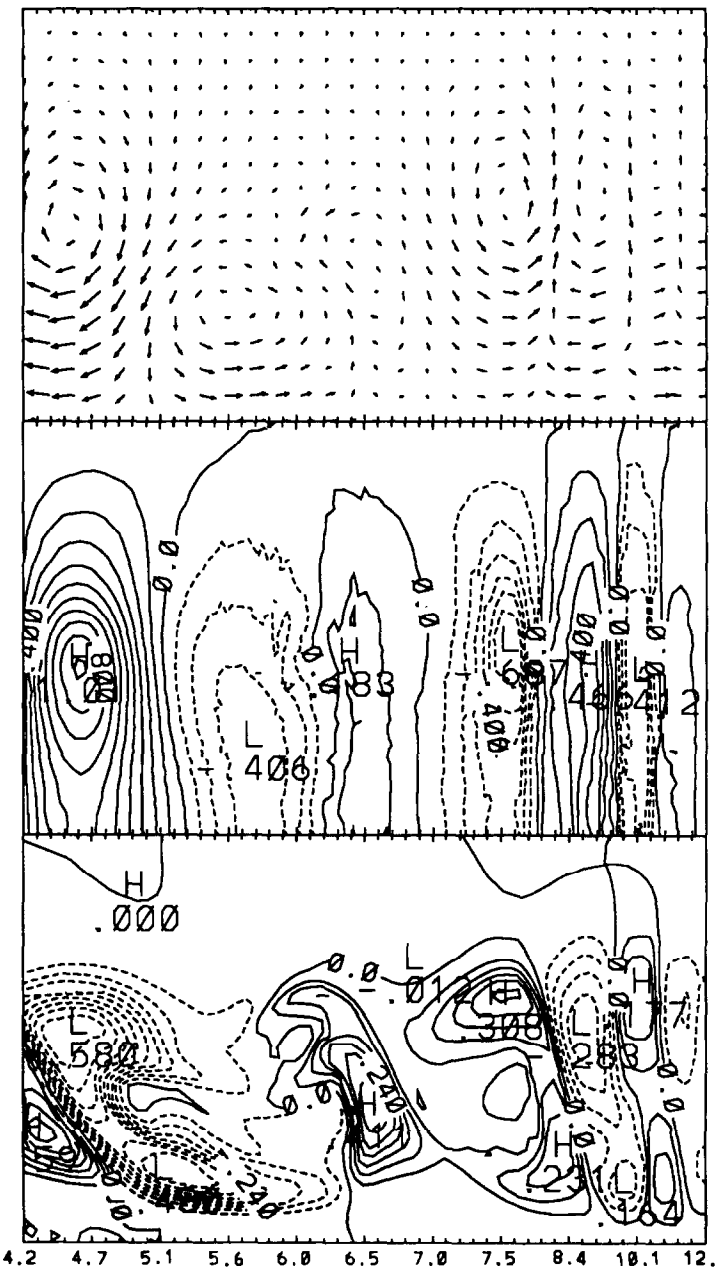

FIG. 4. Top: Fluctuating momentum density field for Fig. 1. Center: Corresponding fluctuating pressure field. Bottom: Fluctuating mass fraction.

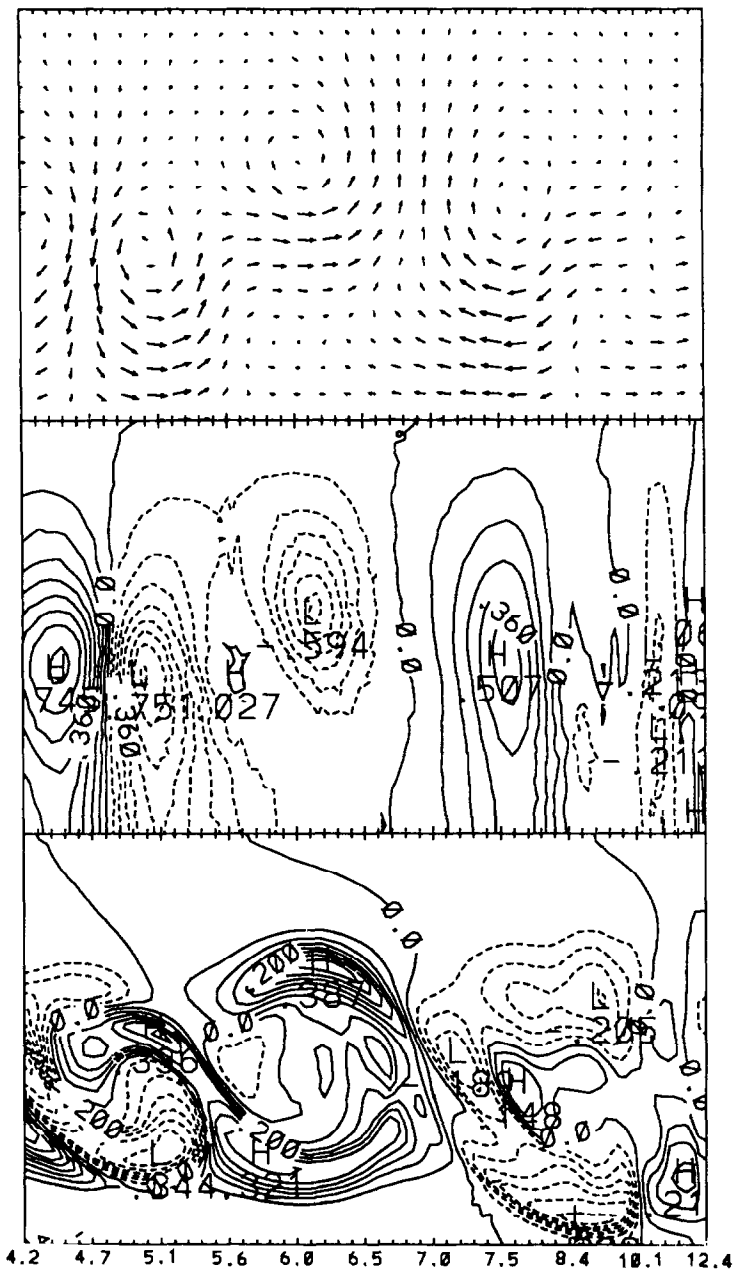

FIG. 5. Top: Fluctuating momentum density field for Fig. 2. Center: Corresponding fluctuating pressure field. Bottom: Fluctuating mass fraction.

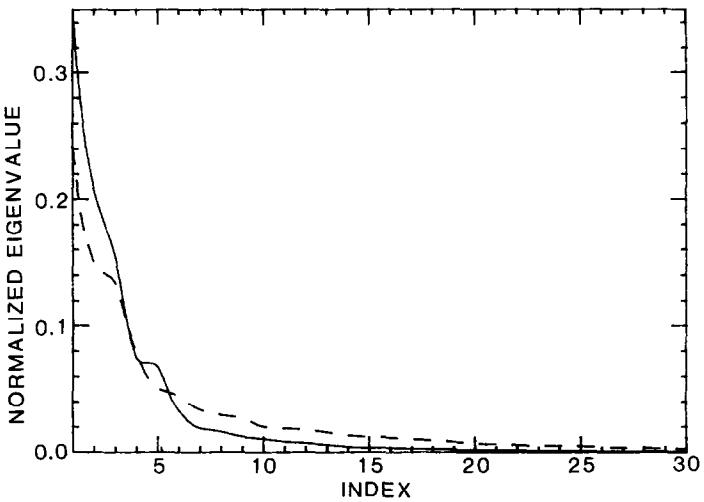

FIG. 6. Normalized eigenvalue $\lambda^{(i)}/\sum_i \lambda^{(i)}$ versus i for the concantenated variable (solid curve) and mass fraction (dashed curve).

220 snapshots, the values of q_N^M decreased only a couple of percent for fixed N as we increased the ensemble from 70 to 220. The quantity $1 - q_N$ corresponds to the

the degree of accuracy required. However, this decision should be made keeping the behavior of the above two figures in mind, since they indicate that there is a identifiable trade-off between accuracy and efficiency. Specifically, consider the solid

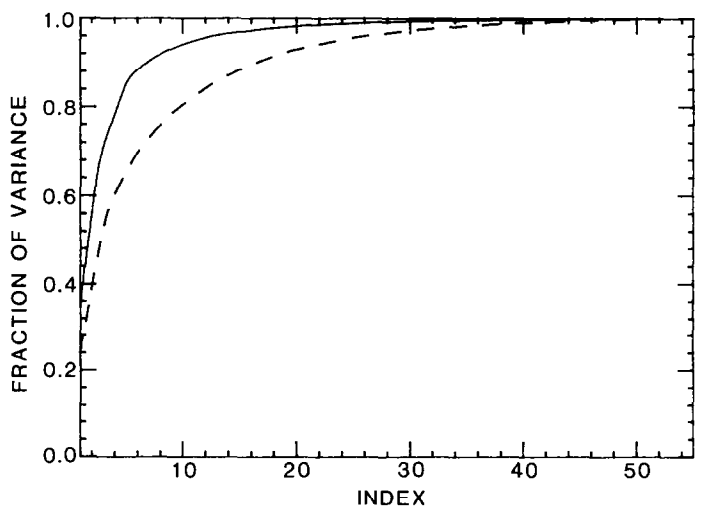

FIG. 7. Fraction of total energy q_N as a function of N for concatenated variable (solid curve) and mass fraction (dashed curve).

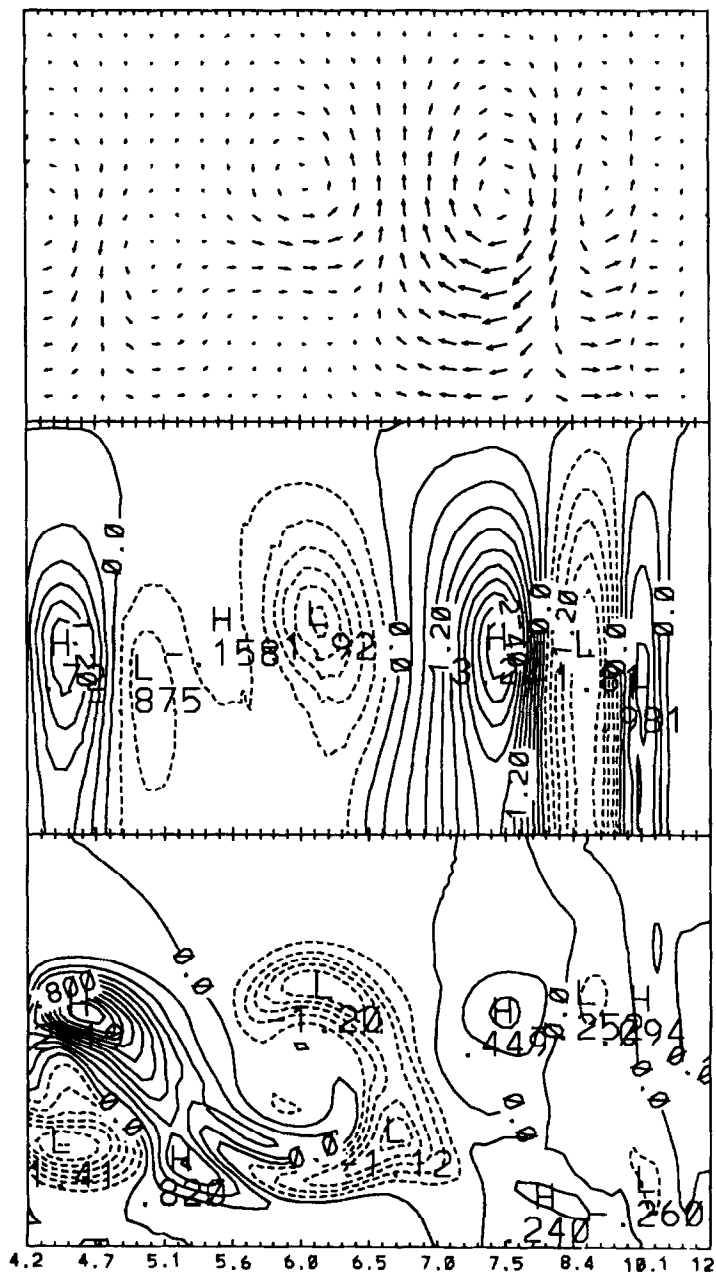

FIG. 8. Eigenfunctions corresponding to largest eigenvalue. Top: Momentum density component. Center: Pressure field component. Bottom: Mass fraction eigenfunction.

curve in Fig. 7. It can be roughly approximated as two piecewise linear segments that join when the eigenvalue index is between 5 and 15. From this we see that it is most efficient to truncate the expansion at the point where the rate of capture of the variance falls off, corresponding to roughly a 5 to 15 term expansion for the composed variable. The error E_N averaged over three flows taken from outside of the ensemble (but still satisfying the strobe condition) supports this interpretation, see upper dashed line in Fig. 10 (top). The slope of the error curve is steep initially and then flattens out at a point corresponding to about 10 terms. There is an analogous behavior for the rate at which the mass fraction expansion captures information. However, the transition region between fast and slow convergence occurs between 10 and 20 terms.

5.3. *Eigenflows*

Interpreting the eigenflows is facilitated since we have knowledge of several flow variables. It should be kept in mind that they are not solutions of the flow, in fact, in general they do not even satisfy the continuity equation (1.1), as in the case of incompressible flow. Hence, while we attribute physical meanings to them, they do not in fact represent physics per se.

The first eigenfunction of the composed variable, shown in Fig. 8, contains 35% of the statistical variance of the flow. The dominating feature is a large vortex structure bounded on either side by a weaker vortex. These weaker vortices are the manifestation of the vortex mergings occurring in the vicinity of the strobe location whose phase with respect to the strobe condition is variable. The centers of the vortices correspond to extrema of the pressure field component of the eigenfunction. Also, the vortex strength is proportional to the magnitude of the corresponding pressure extremum. The first mass fraction eigenfunction contains 24% of the total variance. The extrema located on the interface between the jet and background air correspond to centers of vorticity in the momentum density component.

The second eigenfunction of (4), shown in Fig. 9, containing 21% of the variance, has one dominant vortex, and an associated pressure extremum, located at roughly 4.2 to 5.5 diameters downstream. The corresponding mass fraction eigenfunction has 15% of the variance. There does not appear to be any direct correspondence between this eigenfunction and its counterpart from (4). One might speculate that this might change if there we considered statistically larger ensembles.

Later eigenfunctions are seen to consist of much smaller scale features and possess only a small fraction of the total variance. For example, the 40th eigenflow for the composed variable possesses only 0.03% of the total variance. The associated mass fraction eigenfunction has appreciably larger scale structures, possibly a sign that an ensemble size of 55 for a derived flow variable has deficient statistics. It accounts for 0.10% of the variance. This deficit is probably related to the fact that an interface is particularly difficult to represent by this procedure because it has a continuum of possible locations *but* is sharp in any one realization.

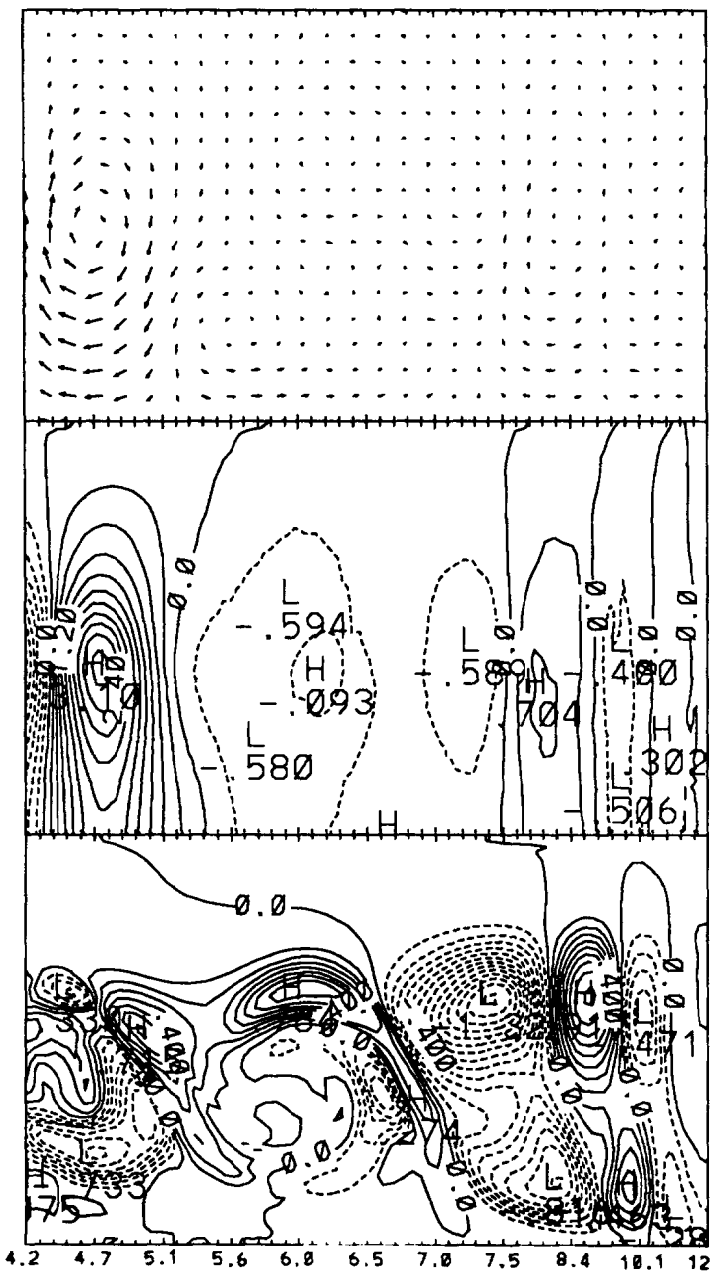

FIG. 9. Eigenfunctions corresponding to second largest eigenvalue. Top: Momentum density component. Center: Pressure field component. Bottom: Mass fraction eigenfunction.

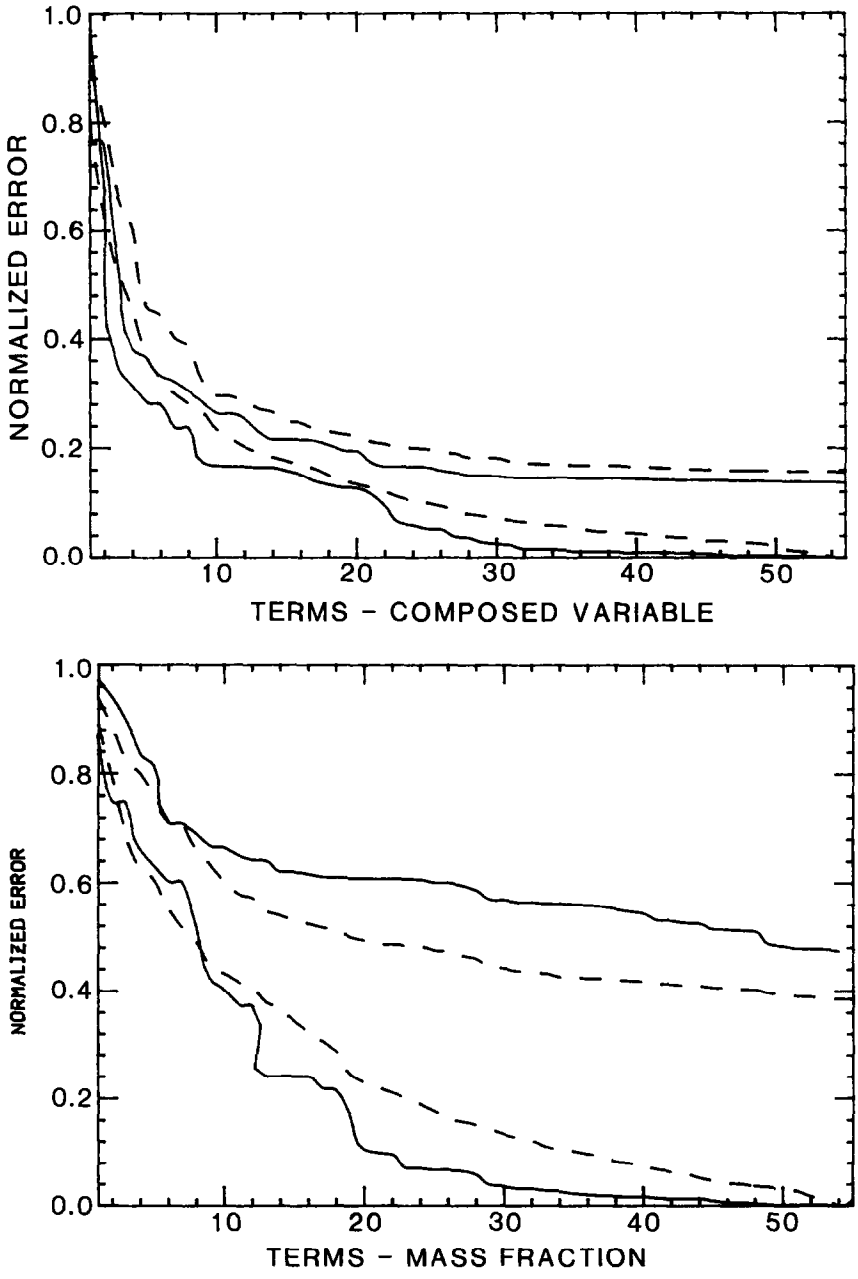

FIG. 10. Top: Approximation errors E_N for composed variable. Lower dashed curve represents error averaged over 11 realizations belonging to ensemble; upper dashed curve represents error averaged over three arbitrary flows not used in the computation of the covariance matrix. The solid curves represent the errors for Fig. 4 (lower) and Fig. 5 (upper). Bottom: Same errors for mass fraction.

5.4. *Reconstructions and Approximations*

To test the extent to which the above procedure results in a low-dimensional description of the flow we project two realizations onto the basis. One, shown in Fig. 4, is used in computing the eigenfunctions. The second, shown in Fig. 5, is not.

In the first case, the reconstruction errors for the composed flow variable are 28% and 16% for 5 and 10 terms, respectively (with respect to the fluctating field). In the second example the approximation errors are 36%, 26%, and 14% for 5, 10, and 55 terms. The errors for the mass fraction are 63% and 40% for the 5 and 10 term reconstruction of Fig. 4 (bottom) and 81%, 67%, and 51% for the 5, 10, and 55 term reconstruction of Fig. 5 (bottom). These numbers are seen to be typical when compared to errors averaged over several flows, see Fig. 10 (note that the errors are considerably smaller when measured with respect to the mean flow field). As might be anticipated from the corresponding eigenvalue spectrums, the

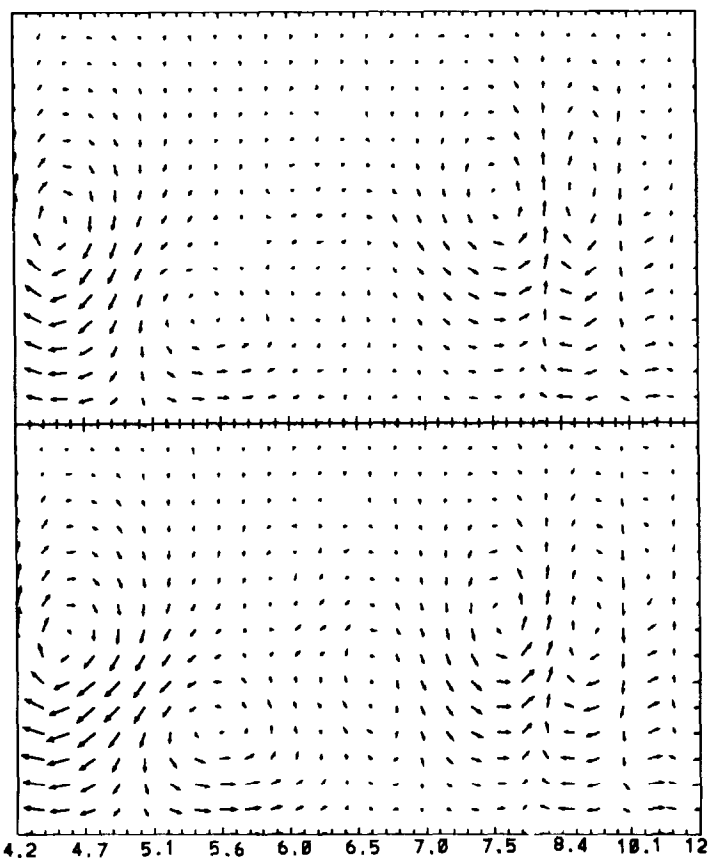

FIG. 11. Reconstruction of the momentum density component of Fig. 4. Top: Five terms. Bottom: 10 terms.

approximation of the mass fraction is not as successful as that for the composed variable. This should be expected in view of the larger estimate of the dimensionality given in 5.2. In this instance the ensemble size is really too small to accurately capture the wide variety of flows described by the mass fraction. In fact a modified procedure might be considered based on the 1D interface location rather than a 2D representation of it.

For flows that belong to the ensemble used in computing the eigenfunctions the errors are relatively small and the contour plots of the reconstructions reflect this, see Figs. 11–13. A more demanding test of the method is the approximation of arbitrary flows that satisfy the strobe criterion. In this case, we saw that quantitatively the errors were reasonable for the composed variable but rather large for the mass fraction. Pictorially, see Fig. 14, the five term reconstruction does a remarkable job in capturing the location and strength of the vortices. The pressure

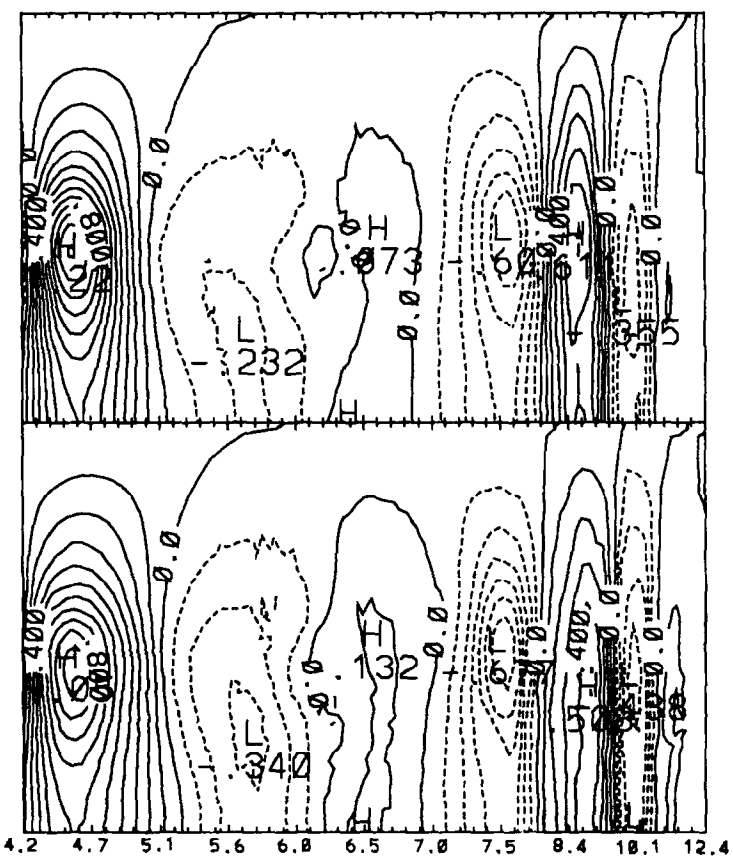

FIG. 12. Reconstruction of the pressure field component of Fig. 4. Top: Five terms. Bottom: 10 terms.

field is similarly well captured (Fig. 15). Despite the fact that the quantitative error of the mass fraction is large, the large scale features are still captured, at least visually.

6. Comparison to the Analysis of Experimental Data

One of the major drawbacks of the application of the snapshot method to numerical data is that the cost of the computations required to obtain sufficient statistics is significant. This is not the case with experimental data obtained for a seeded jet where thousands of realizations may be captured in a matter of seconds [35]. Here the disadvantage is that the type information is limited to concentration fields. In this section, we speculate on the connections between the experimental and machine flow studies. For details of the experiment, see [30].

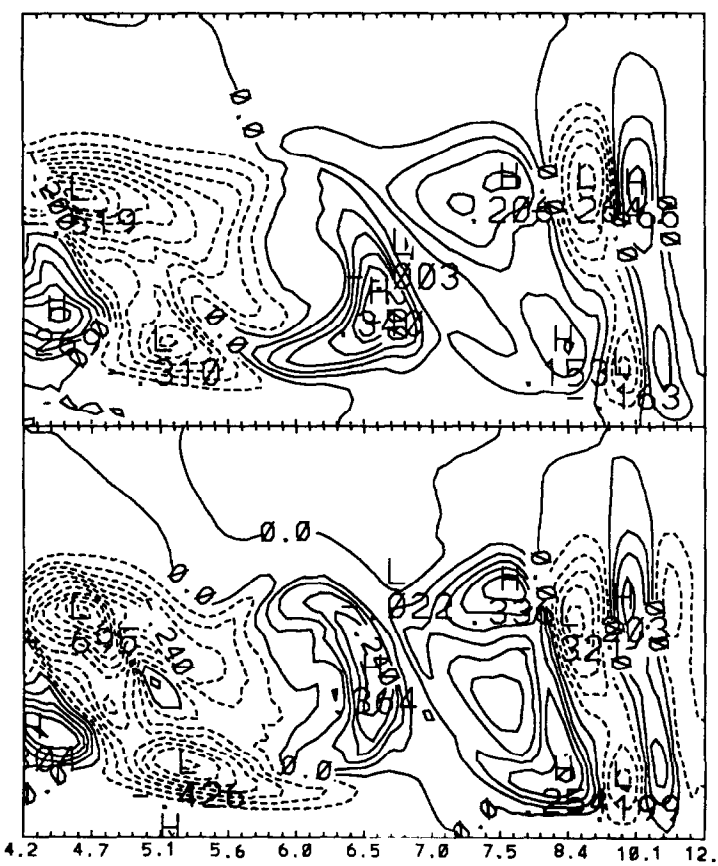

Fig. 13. Reconstruction of the mass fraction component of Fig. 4. Top: Five terms. Bottom: 10 terms.

We show for comparison the first eigenfunction computed from a set of 220 pattern recognized coherent structures obtained for a seeded jet at a Reynolds number of $O(10^3)$, see Fig. 16. The frame of this eigenfunction sits from 5.25 to 8.75 diameters downstream, compared to 4.5 to 12.4 diameters for the numerical data. There are three large scale structures, situated roughly on the edge of the material interface, i.e., a high with a low on either side. This might be optionally interpreted as a low and two highs, since an eigenfunction is only determined to within an arbitrary multiplicative constant. We see this same kind of structure on the material interface of the first mass fraction eigenfunction. The numerical eigenfunction differs in that it has internal structure, largely absent in the experimental eigenfunction. It is tempting to infer from the numerical study that these high–low regions can be directly associated with vortices found in the first eigenfunction.

Obviously, the above results may be important in establishing a connection between the numerical and experimental study, but the analogy suffers from some

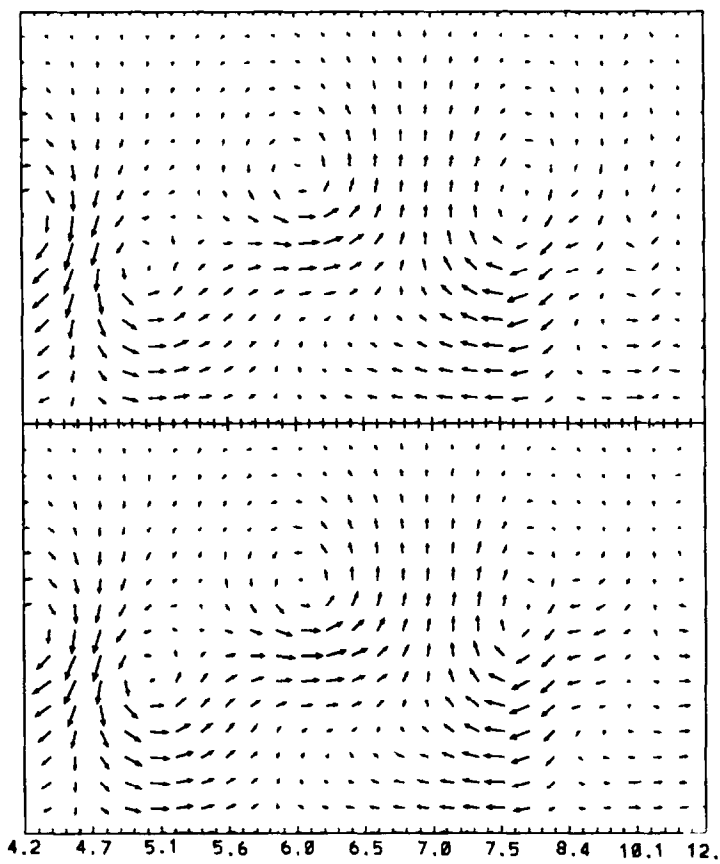

FIG. 14. Approximation of the momentum density component of Fig. 5. Top: Five terms. Bottom: 10 terms.

deficiencies. Differences in the acquisition and sampling of the data (the experiment applies a template fitting procedure), necessarily mean that we are looking at different, although possibly related, large-scale structures. The numerical simulation must be run longer to generate more reliable statistics for the higher order eigenfunctions. Also, as mentioned earlier, we are comparing slices of a fully three dimensional flow (although dominated by 2D effects) at a moderately low Reynolds number to a relatively fast 2D Euler simulation. Nevertheless, the potential of this approach is such that these inferences are reasonable to consider.

7. Discussion

In this study we propose a low dimensional characterization of large scale coherent structures obtained using a conditional sampling procedure. We see that

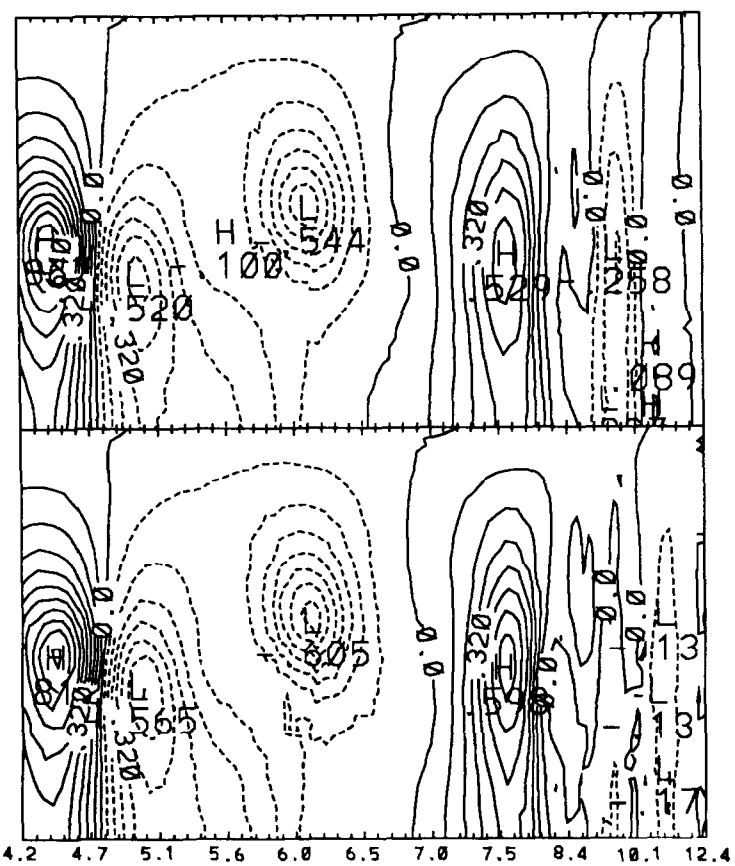

Fig. 15. Approximation of the pressure field component of Fig. 5. Top: Five terms. Bottom: 10 terms.

the large scale features of an arbitrary structure are captured using a small number of terms in a characteristic expansion. The results indicate that the most economic expansions can be determined by the average error slopes which represent the rate of convergence. The importance of the later eigenfunctions is related to the smaller scales of the flow.

The decomposition of the composed variable led to a more accurate description of the primitive variables than the corresponding analysis of the mass fraction. The relative magnitude of the eigenvalues tells us that the mass fraction is exhibiting more complicated behavior than the primitive variables probably because of the physically discontinuous interface involved. Thus a larger ensemble size is required to achieve a more accurate expansion in this case.

We see that the comparison to the experimental data yields positive results but admit that the differences between the two flows and a lack of numerical statistics

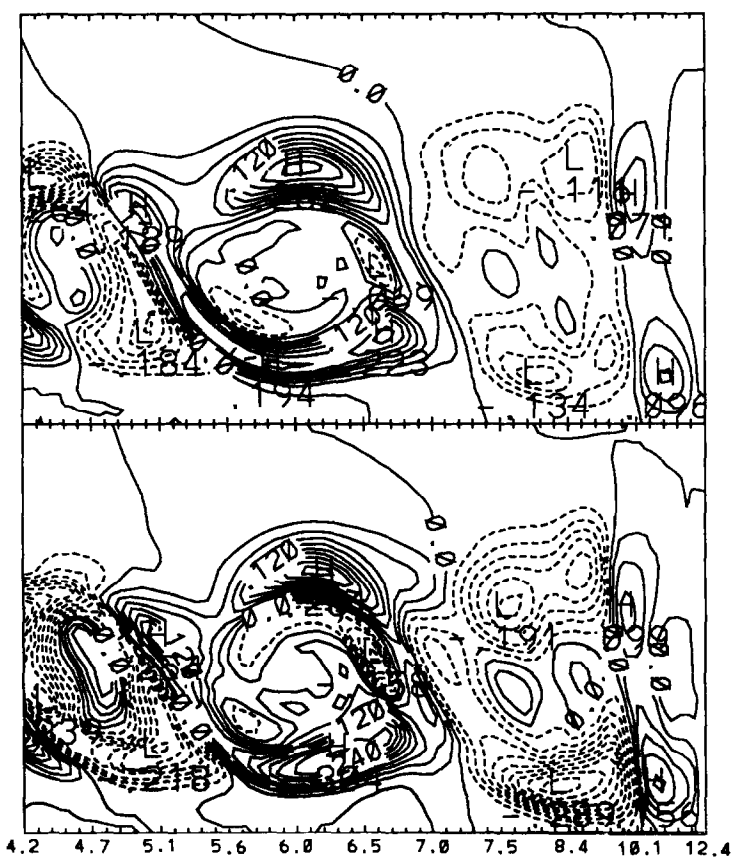

FIG. 16. Approximation of the mass fraction component of Fig. 5. Top: Five terms. Bottom: 10 terms.

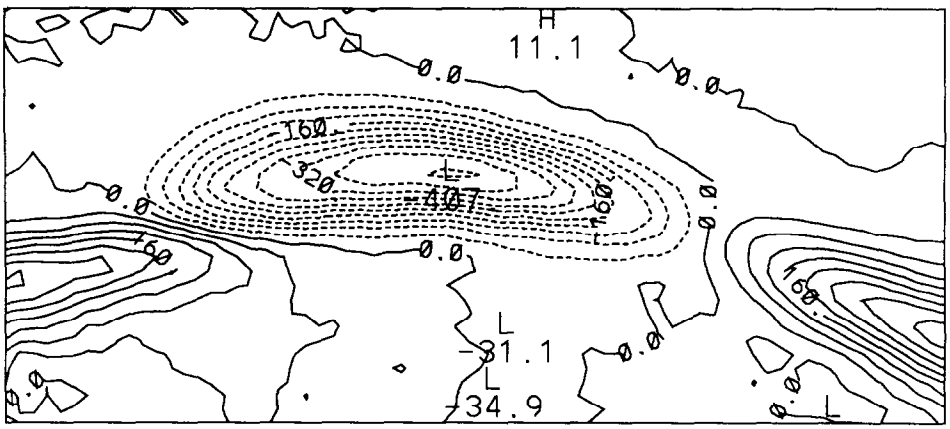

FIG. 17. First eigenfunction of the experimental jet data. Ensemble size = 210, Reynolds number = 1150, field location is 5.25 to 8.75 diameters downstream.

should promote a certain amount of circumspection. However, it seems likely that this type of approach will be beneficial in future applications to three dimensional data, both numerical and experimental.

ACKNOWLEDGMENTS

We would like to thank Michael Winter for many helpful and informative conversations and Theodore Young for his efforts on GAPS and the Reactive Flow Model which made these computations possible. The research reported here was supported in part by DARPA/URI Contract N00014-86-0754.

REFERENCES

1. A. A. TOWNSEND, *The Structure of Turbulent Shear Flow* (Cambridge University Press, Cambridge, 1956).
2. T. THEODORSEN, in *Proceedings, 2nd Midwestern Conference on Fluid Mechanics, Ohio State University, Columbus, Ohio*, 1952.
3. G. L. BROWN AND A. ROSHKO, *J. Fluid Mech.* **64**, 775 (1974).
4. B. J. CANTWELL, *Ann. Rev. Fluid Mech.* **13**, 457 (1981).
5. A. K. M. F. HUSSAIN, *Phys. Fluids* **26**, 2816 (1983).
6. A. K. M. F. HUSSAIN, *J. Fluid Mech.* **173**, 303 (1986).
7. H. E. FEIDLER, in *Proceedings of Advances in Turbulence*, edited by G. Comte-Bellot and J. Mathieu (Springer-Verlag, New York/Berlin, 1987), p. 320.
8. A. K. M. F. HUSSAIN AND K. B. M. Q. ZAMAN, *J. Fluid Mech.* **110**, 39 (1981).
9. K. R. SREENIVASAN, *Phys. Fluids* **21**, 867 (1984).
10. S. C. CROW AND F. H. CHAMPAGNE, *J. Fluid Mech.* **48**, Part 3, 547 (1971).
11. A. J. YULE, *J. Fluid Mech.* **89**, Part 3, 413 (1978).
12. H. BRUUN, *J. Fluid Mech.* **83**, Part 4, 641 (1977).
13. L. SIROVICH, *Q. Appl. Math.* **45**, No. 3, 561 (1987).
14. L. SIROVICH, *Q. Appl. Math.* **45**, No. 3, 573 (1987).

15. L. SIROVICH, *Q. Appl. Math.* **45**, No. 3, 583 (1987).
16. L. SIROVICH, *Phys. D* **37**, 126 (1989).
17. J. L. LUMLEY, in *Atmospheric Turbulence and Radio Wave Propagation*, edited by A. M. Yaglom and V. I. Tatarski (Nauka, Moscow, 1967), p. 166.
18. J. L. LUMLEY, in *Transition and Turbulence*, edited by R. E. Meyer (Academic Press, New York, 1981), p. 215.
19. J. L. LUMLEY, *Stochastic Tools in Turbulence* (Academic Press, New York, 1970).
20. M. N. GLAUSER AND W. K. GEORGE, *European Turbulence Conference* (Lyon, France, 1986).
21. K. FUKUNAGA, *Introduction to statistical pattern recognition* (Academic Press, New York, 1972).
22. H. HOTELLING, *J. Educ. Psychol.*, September 1933.
23. M. M. LOÈVE, *Probability Theory*, (Van Nostrand, Princeton, NJ, 1955).
24. K. KARHUNEN, *Ann. Acad. Sci. Fenn. Ser. A1 Math. Phys.* **37** (1946).
25. S. WATANABE, in *Transactions of the Fourth Prague Conference on Information Theory, Statistical Decision Functions, Random Processes, Prague. August* 31–*September* 11, 1965, edited by academician J. Kozesnik (Academic Press, New York/London), p. 635.
26. R. B. ASH AND M. F. GARDNER, *Topics in Stochastic Processes* (Academic Press, New York, 1975).
27. R. F. BLACKWELDER AND R. E. KAPLAN, *J. Fluid Mech.* **76**, 89 (1976).
28. S. S. LU AND W. W. WILLMARTH, *J. Fluid Mech.* **60**, 481 (1973).
29. R. J. ADRIAN, *Phys. Fluids* **22**, 2065 (1979).
30. L. SIROVICH, M. KIRBY, AND M. WINTER, *Phys. Fluids A* **2**, 127 (1990).
31. E. ORAN AND J. P. BORIS, *Numerical Simulation of Reactive Flow* (Elsevier Science, New York, 1987).
32. F. F. GRINSTEIN, F. HUSSAIN, AND E. S. ORAN, "A Numerical Study of Mixing Control Spatially Evolving Shear Flows," AIAA paper 89-0977, AIAA 2nd Shear Flow Conference, Tempe, Arizona, 1989.
33. J. P. BORIS, in *Proceedings Wither Turbulence? or Turbulence at the Crossroads, Cornell University, March* 1989, to appear.
34. M. KIRBY AND L. SIROVICH, *IEEE Trans.* **12**, 103 (1990).
35. M. WINTER, J. K. LAM, AND M. B. LONG, *Exp. Fluids* **5**, 177 (1987).